Catalytic Water Electrolysis by Co-Cu-W Mixed Metal Oxides: Insights from Operando X-ray Absorption Spectroscopy

Nikita Gupta[1,2], Carlo Segre[3], Carsten Streb[4], Dandan Gao[4]*, Ksenija D. Glusac[1,2]*

[1] Department of Chemistry, University of Illinois Chicago, Chicago, Illinois 60607, United States

[2] Chemical Sciences and Engineering, Argonne National Laboratory, Illinois 60439, United States

[3] Department of Physics & Center for Synchrotron Radiation Research and Instrumentation, Illinois Institute of Technology, Chicago, Illinois 60616, United States

[4] Department of Chemistry, Johannes Gutenberg University Mainz, Mainz 55128, Germany

KEYWORDS: electrocatalysis · mixed metal oxide · active species· X-ray absorption spectroscopy · water-splitting.

ABSTRACT: Mixed Metal oxides (MMOs) are a promising class of electrocatalysts for the oxygen evolution reaction (OER) and hydrogen evolution reaction (HER). Despite their importance for sustainable energy schemes, our understanding of relevant reaction pathways, catalytically active sites and synergistic effects is rather limited. Here, we applied synchrotron-based X-ray absorption spectroscopy (XAS) to explore the evolution of an amorphous Co-Cu-W MMO electrocatalyst, shown previously to be an efficient bifunctional OER and HER catalyst for water splitting. Ex-situ K- and L-edge XAS measurements provided structural environments and the oxidation state of the metals involved, revealing Co^{2+} (octahedral), $Cu^{+/2+}$ (tetrahedral / square-planar) and W^{6+} (octahedral) centers. Operando XAS investigations, including X-ray absorption near-edge structure (XANES) and extended X-ray absorption fine structure (EXAFS), elucidated the dynamic structural transformations of Co, Cu, and W metal centers during OER or HER. The experimental results indicate that Co^{3+} and Cu^0 are the active catalytic sites involved in OER and HER, respectively, while Cu^{2+} and W^{6+} play crucial roles as structure stabilizers, suggesting strong synergistic interactions within the Co-Cu-W MMO system. These results, combined with the Tafel slope analysis, revealed that the bottleneck intermediate during OER is Co^{3+} hydroperoxide, whose formation is accompanied by changes in the Cu-O bond lengths, pointing to a possible synergistic effect between Co and Cu ions. Our study reveals important structural effects taking place during MMO-driven OER/HER electrocatalysis and provides essential experimental insights into the complex catalytic mechanism of emerging noble metal-free MMO electrocatalysts for full water splitting.

INTRODUCTION

Green hydrogen is seen as a promising alternative to carbon-based fuels for use in various energy systems, including combustion engines, turbines, and fuel cells.[1,2] It is produced via water electrolysis, a process that can be expressed in terms of the two half-reactions, namely the oxygen evolution reaction (OER) and the hydrogen evolution reaction (HER). OER is considered as the bottleneck of this process and usually requires high overpotentials. The sluggish OER kinetics arise due to challenges associated with the formation of a weak O-O bond and the orchestrating of four proton-coupled electron transfer steps at the desired potential. Traditionally, precious metal oxide (MO) catalysts, such as RuO_2 and IrO_2, have been used as benchmark OER catalysts with high catalytic activity. However, the high cost and scarcity in nature significantly limit their large-scale deployment.[3] As a result, researchers are exploring earth-abundant MOs based on transition metals such as Co, Mn, Ni or Fe, as promising alternatives.[4–7] Remarkably, these non-noble MOs often perform better when combined into mixed metal oxides (MMOs), where synergetic effects boost the catalytic activity for both OER and HER.[8–14] For example, the Qiao group showed that the presence of Zn and Ni enhances the HER activity of CoO, by providing an ideal environment for intermediate H-binding (by Ni^{2+}) and by boosting the electrical conduction (by Zn^{2+}).[15] In another example, the Nocera group has shown that the incorporation of Fe^{3+} into the nickel oxide (NiO) matrix increases the ability of the catalyst to access Ni^{4+} state, thus enhancing the OER performance.[11] Furthermore, the employment of MMOs as bifunctional catalysts also has the potential to simplify the catalyst design and fabrication, reduce cross-contamination, and prevent catalyst poisoning, making it an attractive option for the production of green hydrogen.

A comprehensive understanding of the catalytic mechanism of MMOs for OER and HER is being actively explored. Based on computational works, the OER in an alkaline medium is generally considered to occur via one of the two mechanistic pathways.[16–19] Pathway I, known as the adsorbate evolution mechanism, involves a single active site, in which the activity is strongly correlated with the adsorption energies of the M-O intermediates. This pathway includes the formation of adsorbed M-OH species on the catalyst surface, their subsequent transformation to M-OOH, and the eventual release of O_2.[20–22] While pathway II, known as the lattice oxygen evolution mechanism, involves the participation of lattice oxygen in the oxide catalyst during O-O coupling and OER.[23,24] This pathway includes the direct combination of two M-O species, leading to O_2 formation and the generation of active species. Similarly, the HER can occur via one of two reaction pathways, both of which involve electrochemical hydrogen adsorption as the first step in the catalytic reaction. In this context, pathway I proceeds via an electrochemical desorption step, which is known as the Volmer-Heyrovsky mechanism. While pathway II, known as the Volmer-Tafel mechanism, proceeds via H-H bond formation and chemical desorption route.[24,25] These mechanisms are analogous to the adsorbate evolution mechanism and lattice oxygen evolution mechanism in the case of OER, respectively. Furthermore, various descriptors have been proposed in the literature to correlate OER and HER activity, including the bond strengths of the bound M-OH and M-O intermediates,[26–29] the exchange current density,[30–32] the count of 3d electrons in the metal ion,[29,33,34] the number of unsaturated sites,[35,36] or the energy gap between O p-band relative to the Fermi level.[37] The use of descriptors greatly simplifies the understanding of metal oxide activity trends.

Additionally, the precise identification of catalytically active sites of MMOs electrocatalysts is also attracting substantial attention. In this regard, ex-situ characterization techniques can provide information regarding the atomic and electronic structures of the electrocatalyst pre- and post- catalytic OER / HER, while the operando investigation can shed light on the dynamic evolution of focused active sites over the catalytic process.[38,39] To this end, several different in-situ/operando characterization techniques have been used to study OER processes, such as surface interrogation-scanning electrochemical microscopy (SI-SECM),[40] transmission electron microscopy (TEM),[41,42] Raman spectroscopy,[19,43] Fourier transform infrared spectroscopy (FTIR),[44] X-ray diffraction (XRD),[45–47] ambient pressure X-ray photoelectron spectroscopy (APXPS),[48] Fe Mössbauer spectroscopy,[49] Resonant Inelastic X-ray Scattering (RIXS),[50] and electrochemical quartz crystal balance (EQCM).[51–53] In comparison to these techniques, X-ray absorption spectroscopy coupled with electrochemistry (XAS-EC) offers unique advantages in probing the chemical, electronic, and structural information of electrocatalysts. With XAS-EC, oxidation states, coordination environments, bond strengths, and catalytic intermediates of absorbed atoms on active species can be studied to gain real-time insight into molecule-based catalytic mechanisms under operating conditions.[19,47,54–56] In one instructive example, studies by the Abruna group identified the active sites as $Co^{2+/3+}$ and $Mn^{2+/3+/4+}$ redox couples for a bimetallic $Co_{1.5}Mn_{1.5}O_4$/C catalyst system for OER and commented on the synergistic effect of Mn and Co.[57] In another example, the Boettcher group revealed the partial Fe oxidation and a shortened Fe-O bond length during OER on the synthesized $Co(Fe)O_xH_y$ electrocatalyst, while only Co oxidation was observed in the absence of Fe cation, indicative of the essential role of Fe cation for OER.[58]

In this study, we delve into the structural dynamics of a versatile bifunctional electrocatalyst developed by the Streb group,[59] specifically the Co-Cu-W mixed metal oxide (Co-Cu-W MMO) electrocatalyst that was formed by the hydrothermal reaction involving Co-ions, Cu-foam and a polyoxometalate precursor as W-source ($[SiW_{11}O_{39}]^{8-}$, Scheme 1). The obtained Co-Cu-W MMO was found to be an outstanding bifunctional electrocatalyst for both OER and HER, with stable activity over prolonged time (>10 h). Furthermore, the electrocatalysis was highly efficient: for OER, the overpotential (at j = 10 mA/cm^2) was 313 mV and the Faradaic efficiency was ~ 100 %; for HER, the overpotential (at j = 10 mA/cm^2) was 103 mV and the Faradaic efficiency was ~ 98 %. However, to-date, the underlying electrochemical OER and HER mechanisms which enable this performance by the Co-Cu-W MMO remain unexplored.

Here, employing cutting-edge X-ray absorption spectro-electrochemistry (XAS-EC) at the Co and Cu K edges, as well as W L_3 edge, we uncover the intriguing structural transformations of this MMO that occurs during water splitting. Through X-ray absorption near-edge structure (XANES), we gain precise knowledge regarding the oxidation states of the constituent metals, while extended X-ray absorption fine structure (EXAFS) unveils the structural changes of each metal center over electrocatalysis. In combination with Tafel slope analysis to derive information regarding the rate-determining step, these data allow us to propose plausible mechanisms for OER and HER catalysis by the Co-Cu-W MMO. The OER was found to predominantly occur at the Co-center, generating Co^{3+}-OOH as a bottleneck intermediate that undergoes a rate-determining release of molecular oxygen. Importantly, we have also identified interesting structural changes that take place at the neighboring Cu-centers. While Cu does not undergo a change in the oxidation state, we discovered a lengthening of Cu-O bonds at Cu centers adjacent to Co^{3+}-OOH intermediates, which points to a possible synergistic role of the Cu-atoms to stabilize the Co^{3+}-OOH intermediates. These results shed light on the likely mechanism by which the Co-Cu-W MMO achieves high OER performance and provides target catalytic motifs for future molecular engineering of bimetallic electrocatalysts. Under cathodic HER conditions, our Cu K-edge XAS-EC results provides strong evidence for the formation of metallic Cu nanoparticles (Cu-NPs) whose diameter increase during electrolysis, reaching final values of ~9 Å.

SCHEME 1. Hydrothermal synthesis of Co-Cu-W MMO.

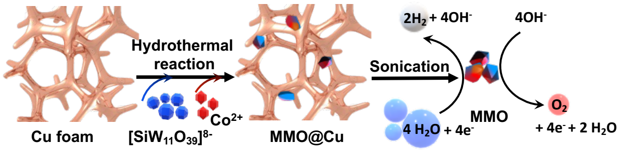

RESULTS AND DISCUSSION

Ex-situ XAS: To comprehensively investigate the oxidation states and coordination environments of Co, W and Cu elements in the MMO, ex-situ XANES and EXAFS were performed. To this end, two model polyoxometalates (POM) were synthesized as references: POM1 ($Na_{10}[Co_4(H_2O)_2(PW_9O_{34})_2]$, Figure 1a) containing Co^{2+} and W^{6+} and POM2 ($Na_5[CoW_{12}O_{40}]$, Figure 1b) containing Co^{3+} and W^{6+}.[60–62] Synthetic routes and characterization details, see supporting information (SI) and Figure S1. As shown in Figure 1c, the ex-situ Co K edge XANES spectra of POM1 demonstrate weak pre-edge features at 7710.6 eV and an edge energy of 7719 eV. Additionally, the pronounced white line characteristic implies a octahedral (O_h) coordination environment for the Co ions in POM1.[58] In contrast, POM2 exhibits distinct spectral features with a strong pre-edge peak (i: 7710.5 eV, assigned to the $1s \rightarrow t_{2g}$ transition) and a weak peak (ii: 7716.0 eV, assigned to the $1s \rightarrow e_g$ transition), indicative of a non-centrosymmetric tetrahedral (T_d) arrangement of the Co ions in POM2.[58] Furthermore, POM2 displays a visible rising edge peak (iii: 7722.5 eV, $1s \rightarrow 4p$) with an edge energy of 7720.5 eV. These geometry assignments are consistent with the previously reported XANES of relevant Co-complexes (e.g., $Na_{10}[Co_4(H_2O)_2(VW_9O_{34})_2]\cdot 35H_2O$, $K_5[CoW_{12}O_{40}]\cdot 20H_2O$).[60–62]

The Co K edge spectrum of the MMO (Figure 1c) is free of the strong pre-edge features existing in POM2, while it shows substantially matching edge energy (7719 eV) and white line peak energy to those of POM1, indicative of Co^{2+} oxidation state and O_h geometry of the Co ions in the MMO. According to Figure 1d, the ex-situ XANES W L_3 edge spectra of the MMO shows an edge energy of 10204.6 eV, which is nearly identical to that of W^{6+} containing references POM1, POM2 and WO_3 and significantly different from the W^{4+} reference WO_2. In addition, the broad white line feature shown in POM1, POM2 and WO_3[63,64] was also observed in MMO, demonstrating the O_h coordination geometry of the W in W^{6+} oxidation state. The ex-situ XANES Cu K edge spectrum of MMO shows a sharp edge peak (1s→4p) at 8981.4 eV (labeled as iv, inset Figure 1e) and the absence of the pre-edge peak features existing in the Cu^{2+} reference (CuO, 8979 eV, 1s→3d).[65] Additionally, the MMO shows an edge energy of 8985 eV, which is between that of Cu^{+} (8984 eV) and Cu^{2+} (8986 eV),[66,67] suggesting the presence of a mixture of Cu^{+} and Cu^{2+} in the MMO. This is further confirmed by the linear combination analysis, giving a ratio of 4:1 (Cu^{+}:Cu^{2+}, Figure 1f, Table S1).[68]

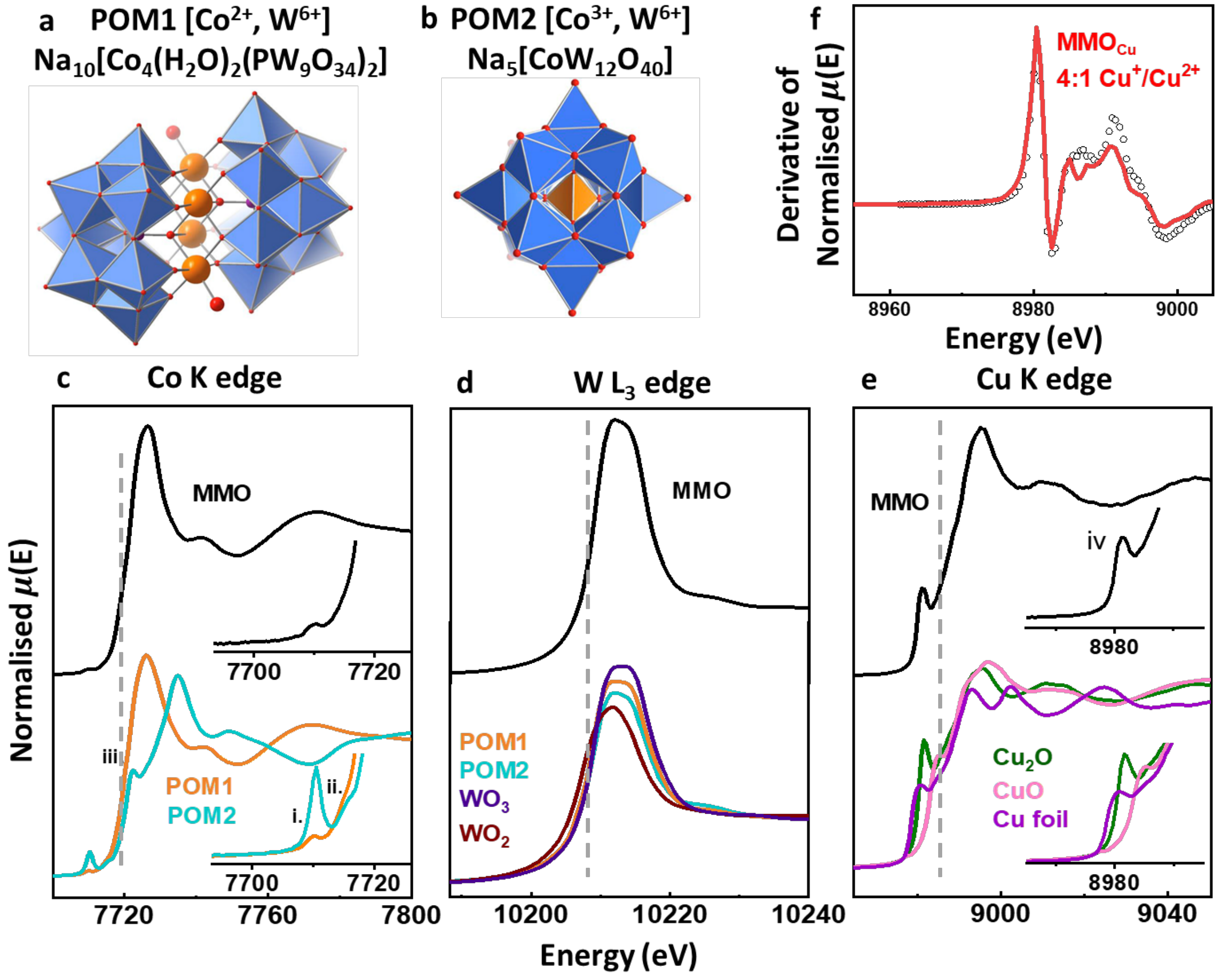

Figure 1. (a) and (b) Structures of POM1 and POM2, color scheme: Co atoms in orange, O in red and W in blue. Ex-situ XANES spectra of (c) Co K edge, (d) W L_3 edge, (e) Cu K edge of MMO and references, where vertical dash line represents the edge energy. (f) Linear combination analysis of the MMO at Cu K edge.

The experimental ex-situ EXAFS data obtained for POM1 and POM2 at the Co K and W L_3 edges were fitted with good-to-excellent results using scattering paths based on their structures obtained previously via single-crystal X-ray diffraction (R- and K-space fitting of POM1 and POM2 data are shown in Figures S2-S3, Table S2).[62,69,70] The dominant interaction in both POM1 and POM2 are the metal-oxygen scattering paths with average bond lengths of 2.019 (n=2), 2.086 (n=2), 2.258 Å (n=2) in POM1 and 1.805 Å (n=4) in POM 2 (n: the number of scattering paths). This highlights the critical role of the metal-oxygen coordination environment in shaping the overall structural characteristics of both model POMs. Furthermore, an in-depth analysis of second shell fitting of POM1 revealed intense Co-Co scattering at 3.2 Å and weak Co-W scattering at 3.5 Å, indicating the presence of neighboring Co and W atoms. In contrast, a pronounced Co-W scattering at ca. 3.5 Å was observed in POM2, consistent with the exclusive Co-W environment.

Following the structural studies of model POMs, we investigated the ex-situ Co K edge, Cu K edge, and W L_3 edge EXAFS spectra of the MMO (Figure 3 and Table 1). The first shell of the Co K edge EXAFS data for MMO was successfully fitted using an O_h CoO_6 geometry with a Co-O bond length of 2.07 Å. In addition, the second coordination shell revealed two distinct scattering paths, Co-X at distances of 2.89 Å (n = 2) and 3.06 Å (n = 6). The identity of X can either be Co or Cu, as both metals have similar atomic numbers and therefore gave equally good fits to the experimental data (Figure S4 and Table S3).[71] Notably, no Co-W scattering was observed in the Co K-edge EXAFS, which is either due to a small number of neighboring W-atoms (similar to the EXAFS of POM1, Figure 2a), or a completely W-free environment.[70–72]

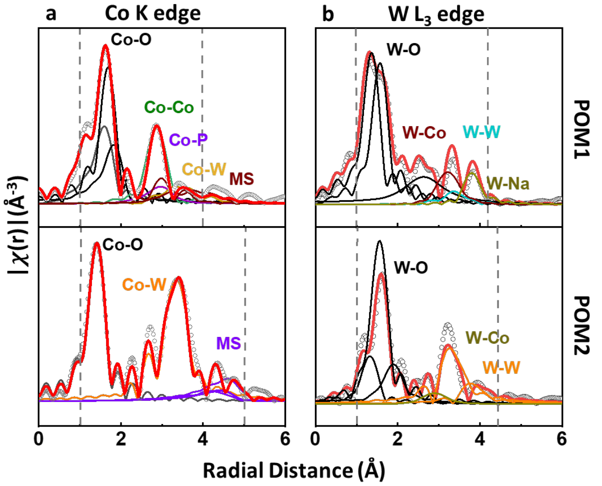

Figure 2. Ex-situ EXAFS of POM references. (a) Co K edge of POM1 (top) and POM2 (bottom), (b) W L_3 edge of POM1 (top) and POM2 (bottom), where the experimental data is in circles and fitted data is the red solid line. Individual path lengths are shown with solid lines. MS: multiple atoms scattering paths.

The Cu K-edge EXAFS data were fitted using a 1:4 combination of two types of Cu environments, in agreement with the presence of Cu^{2+} (20%) and Cu^{+} (80%) ions revealed in the XANES Cu K-edge results. The first shell of Cu^{+} species was modeled as T_d CuO, while the Cu^{2+} species was modeled as square-planar (SP) Cu_2O, and the Cu-O bond lengths obtained from the fit were 1.85 Å ($n = 3$) and 1.96 Å ($n = 1$), respectively, which is in line with literature reports on comparable samples.[72,73] Additionally, the secondary coordination sphere fitting revealed two distinctive Cu-X peaks with bond lengths of 3.00 Å ($n = 6$) and 3.12 Å ($n = 3$) (here, X=Co or Cu, Figure S5 and Table S4, SI).

The EXAFS analysis at the W L_3 edge was performed using an O_h WO_6 first shell with two bond lengths at 1.88 Å ($n = 3$) and 3.01 Å ($n = 3$, Figure 3c). This observation implies the existence of either two distinct WO_6 O_h environments in a 1:1 ratio or one distorted trigonal prismatic configuration. The trigonal prismatic configuration of WO_6 is rare, but it has been observed in mixed metal oxides with AABB packing arrangement of metal-oxo clusters.[74] Moreover, the presence of a second metal site (possibly Co or Cu) was detected at a distance of 3.37 Å (n=2). Notably, no W-W scattering paths were observed, suggesting that all W atoms in the MMO are isolated and surrounded by Co or Cu metal oxides (Figure S6 and Table S5). These extensive ex-situ characterizations lay a solid foundation for subsequent operando XAS studies, which will contribute to an in-depth understanding of the dynamic structural evolution of MMO as well as the potential catalytic mechanism.

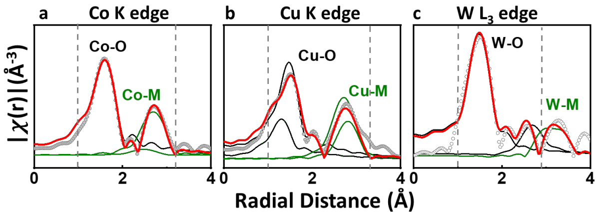

Figure 3. EXAFS data fitting of (a) Co K edge, (b) Cu K edge, and (c) W L_3 edge of MMO where the experimental data is in circles and fitted data is the red solid line. Solid grey dash lines show the data window that have been fitted. Metal-oxygen scattering is shown in black and metal-metal scattering is shown in green.

Table 1. Summary of structure information of MMO.

	Co K edge	Cu K edge	W L_3 edge
Oxidation state	Co^{2+}	Cu^{+}/Cu^{2+}	W^{6+}
Geometry	O_h	T_d / SP	O_h
Fitted bond lengths (X = Cu, Co)	Co-O:	Cu-O:	W-O:
	2.07 Å	1.85 Å, 1.96 Å	1.88 Å, 3.01 Å
	Co-X:	Cu-X:	W-X:
	2.89 Å, 3.06 Å	3.00 Å, 3.13 Å	3.37 Å

XAS-EC: Prior to the XAS-EC studies, the electrocatalytic performance of the solid-state MMO (drop-casted on carbon paper, MMO@CP) was examined for both HER and OER in alkaline aqueous electrolyte (0.1 M aqueous KOH, pH 12.8). Linear sweep voltammetry (LSV) polarization curves (Figure 4a, c) show that the MMO@CP exhibits the suitable electrocatalytic activity, with overpotentials of 365 mV and 447 mV for HER and OER at a current density j of 10 mA/cm^2 (based on geometric surface area). The overpotential is somewhat higher than the previously reported composite electrode (MMO@Cu),[59] which we attribute to the different electrode support (CP instead of Cu), resulting in a less ideal electrode/catalyst interaction. However, for the targeted XAS study, the increased overpotentials do not pose a problem.

To assess the long-term stability of the MMO@CP, chronoamperometry was conducted over 5 h. The current density was stable under both HER and OER conditions and the comparison of LSV curves before and after 5 h of electrolysis (Insets in Figure 4b, d) displayed nearly identical performance. The current density for HER exhibited an initial increase, hinting at the possible electrochemical generation of the catalytically active species (Figure 4b). The OER activity remained at 82% activity after the 5 h period (Figure 4d), demonstrating the stability of the MMO@CP model electrode under harsh oxidative electrocatalytic conditions.[27]

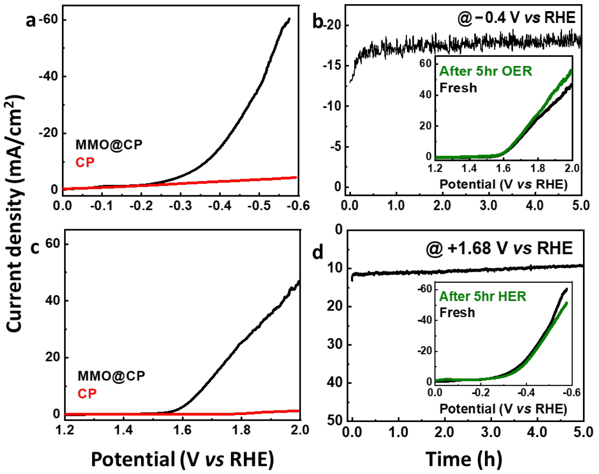

Figure 4. Catalytic performance of MMO@CP for HER and OER. LSV polarization curves of MMO@CP and CP reference for HER (a) and OER (c), scan rate: 5 mV/s; chronoamperometric studies of (c) HER (-0.4 V *vs* RHE) and (d) OER (+1.68 V *vs* RHE); inset: LSV comparison of HER and OER performance.

To gain critical insights into the structural evolution of the MMO under operating conditions, the XAS-EC measurements were conducted at open circuit potential (OCP) and electrocatalytic potentials (+1.68 V *vs* RHE for OER and -0.4 V *vs* RHE for HER) using a custom-built spectro-electrochemical cell (Figure S7, SI). The Co K edge XANES spectra observed under OER conditions (Figure 5a) show a noticeable positive shift of the edge energy (from 7719 eV to 7722 eV), indicative of the oxidation of Co^{2+} to Co^{3+}. This transformation is further supported by the oxidation state analysis involving the integration of the XANES area under the edge from $\mu = 0.1$ to 1 (Figure S8, SI).[75] Additionally, the increase in the intensity of the pre-edge peak (7711 eV, s → d, Figure 5a inset) is expected for the loss of a 3d electron during the Co^{2+} to Co^{3+} oxidation. The increased pre-edge intensity is also considered as a reporter of a deviation from the centrosymmetric O_h geometry. This reduction in symmetry is known to lead to increased 3d–4p hybridization of the metal orbitals, thus increasing the "allowedness" of the 1s → 3d transition.[76,77] In contrast, under HER condition, no edge energy changes were observed, indicating that the original Co^{2+} oxidation state is retained. The increased pre-edge peak intensity and the expansion of the white line region demonstrates a change in the coordination environment around the Co site during both OER and HER, suggesting that Co sites play an active role during both catalytic processes.

The Cu K edge XANES spectra (Figure 5b) exhibit no significant changes in pre-edge and edge energies (from 8985 eV to 8984.9 eV) during OER, implying that no oxidation state changes occur at the Cu centers during OER. In contrast, a shift of the Cu edge energy to lower values (from 8985 eV to 8984.5 eV, Figure S9, SI) was observed during HER, implying the reduction of Cu^{+}/Cu^{2+} ions to metallic Cu species. Linear combination analysis of these scans also indicated the formation of metallic Cu (from 0 to 62.9%), while the Cu^{+} was found to be diminished (from 80% to 21.6%) and Cu^{2+} slightly decreased (from 20% to 15.5%) (Table S6, Figure S10, SI). This dynamic transformation suggests that the Cu^{+} sites are the pre-catalytic species that are electrochemically reduced to the catalytically active Cu-NPs.

The W L_3 edge XANES spectra displayed no discernible changes in either OER or HER (Figure 5c). The stability of the W sites implies that these sites might act as a redox-inactive spectator which provides structural support to the OER/HER active Co and Cu sites. Furthermore, the absence of significant changes in the W coordination environment observed by the retained broad white line features, indicates that the W atoms remained isolated and surrounded by Co or Cu metal oxide species. For a summary of the structural changes of Co, Cu and W in the MMO, see Table S7.

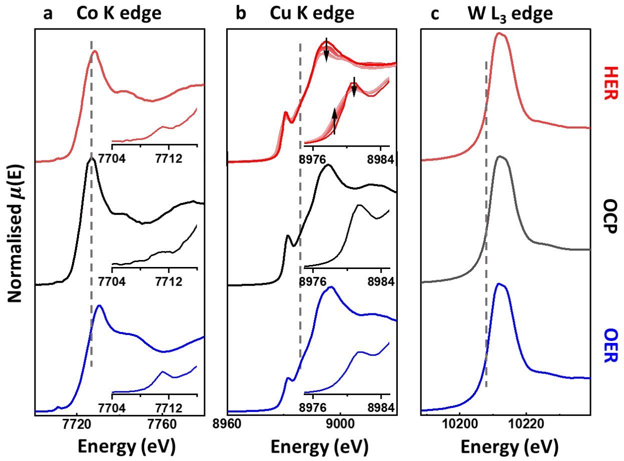

Figure 5. XAS-EC XANES spectra of (a) Co K edge, (b) Cu K edge, (c) W L_3 edge of MMO under -0.4 V *vs* RHE (for HER), 0 V *vs* RHE (for OCP) and +1.68 V *vs* RHE (for OER). The insets show the pre-edge region of the corresponding curves.

Next, XAS-EC EXAFS measurements were performed to capture the local structural evolution of the MMO during electrocatalytic water splitting. Analysis of the Co K edge EXAFS during OER implies the retention of the O_h geometry and the shortening of the Co-O bond length from 2.07 Å to 1.9 Å, along with a decrease in distance for one of the Co-X pathways (from 3.06 Å to 2.9 Å, Figure 6a). Under HER conditions, the O_h coordination environment of Co undergoes a distortion characterized by a pronounced elongation of the two axial Co-O bonds (from 2.07 Å to 2.27 Å), while the length of the four equatorial Co-O bonds remains unchanged. Simultaneously, there was an increase in the Co-X bond length from 2.89 Å to 3.56 Å ($n = 2$), and 3.06 Å ($n = 6$) to 3.25 Å ($n = 4$) (Table S8, Figure S11).[78]

The analysis of the Cu K edge EXAFS spectra during OER shows that the both Cu moieties remain in the original coordination environment, with Cu-O bond lengths increasing from 1.85 Å to 1.93 Å ($n = 3$, Cu^{+}), and from 1.96 Å to 2.16 Å ($n = 1$, Cu^{2+}, Figure 6b). Furthermore, the bond length for Cu-X decreases from 3.0 Å ($n = 6$) to 2.59 Å ($n = 6$), and from 3.12 Å ($n = 3$) to 2.26 Å ($n = 2$), see Table S9 and Figure S12. More drastic EXAFS changes were observed during HER, where Cu species underwent a compositional transformation to metallic Cu-NPs, observed as the growth of the new Cu-Cu scattering feature at 2.7 Å (Figure 6b). This feature grows with electrolysis time from $n = 0$ to 7 over the period of 4 scans. We assign this to the operando formation of metallic Cu-NPs under reducing electrochemical conditions. The size of these Cu-NPs was evaluated based on the number of Cu-Cu scattering paths, using the calibration curve obtained for Cu-Cu scattering in NPs with known diameters, reported in the previous studies.[79–81] We find that the Cu-NP diameter increases over the time of XAS-EC scans, reaching approximately 9 Å (a cluster of ~ 97 Cu atoms, SI) at the end of 4th scan (Table S10 and Figure S13).

Based on the W L_3 edge EXAFS spectra (Figure 6c), the O_h coordination environment around W became more distorted during both OER and HER. OER was accompanied by the decrease in one W-O bond length from 3.01 Å (n=3) to 2.46 Å (n=1) and 2.83 Å (n=2), while the other remained constant within the error limit (1.88 Å (n=3)). In contrast, the length of one W-O bond was reduced from 3.01 Å (n=3) to 2.35 Å (n=1) under HER conditions, while the other W-O bond lengths (1.88 Å (n=3) and 3.01 Å (n=2)) remained unchanged (Table S11 and Figure S14). No significant changes in W-X bond lengths were observed.[78]

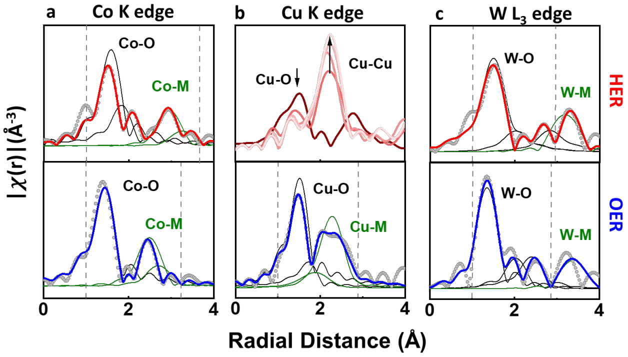

Figure 6. XAS-EC EXAFS measurement of (a) Co K edge, (b) Cu K edge, (c) W L_3 edge of MMO@CP under -0.4 V *vs* RHE (for HER in red), 0 V *vs* RHE (for OCP in brown), and +1.68 V *vs* RHE (for OER in blue). Grey line: M-O scattering, green line: M-M scattering, vertical dash line: r region of R space used for fitting, grey circles: experimental data.

Mechanisms: Insights into HER and OER mechanisms were obtained by combining electrochemical Tafel slope analysis and XAS-EC data fitting. For HER, Tafel slopes exceeding 120 mV/decade (theoretical limit for Tafel slope analysis for HER), were obtained for the MMO@CP (142-208 mV/decade, Figure S15a), while even higher Tafel slopes were observed in the previous study on the composite MMO@Cu electrode (335 mV/decade).[59] Notably, such high Tafel slopes have been reported for HER in basic media, where the water dissociation step ($H_2O \rightarrow H^+ + OH^-$) was proposed as the rate-determining step (RDS).[82–84] As aforementioned, the XAS-EC data of the MMO displayed notable changes in the Cu center during HER, indicating the formation of Cu-NPs (Table S6). Based on these findings, we propose a mechanism that involves the electrochemical conversion of Cu^+-oxo pre-catalyst to catalytically active Cu-NPs, whose protonation to form surface Cu-H species is the RDS (Figure 7). The subsequent H_2 releasing step may occur either via Heyrovsky or Tafel pathways. The established reactivity of Cu-NPs in the literature further supports this observation.[85–87] It is likely that the nanostructured Cu sites exhibit improved HER kinetics via exposing more active sites on the metal surface.[88]

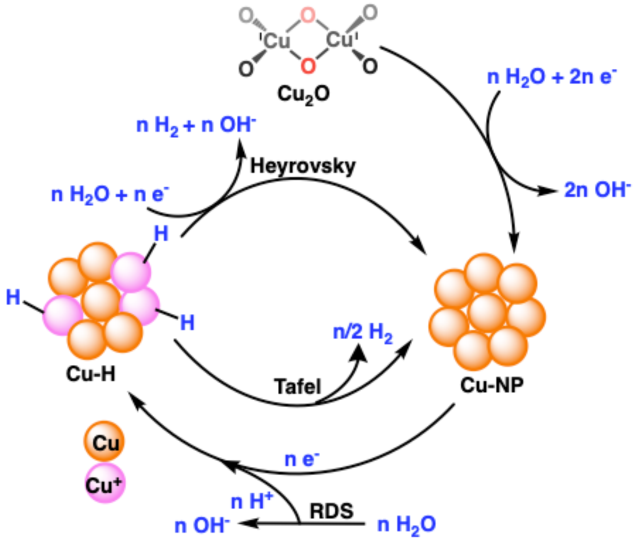

Figure 7. Proposed mechanism for HER by operando formed Cu-NPs on the MMO electrocatalyst.

For OER, the Tafel slopes were derived for two possible OER mechanisms: the single-site (SS) and the double-site (DS) models.[89] Both mechanisms involve the formation of M-OH and M=O intermediates on the MMO surface, where M denotes an active site on the surface of the MMO catalyst:

$$M + OH^- \rightarrow M - OH + e^- \qquad \text{(Step 1)}$$

$$M - OH + OH^- \rightarrow M = O + H_2O + e^- \qquad \text{(Step 2)}$$

The SS model proceeds via the formation of MOOH intermediate:

$$M = O + OH^- \rightarrow MOOH + e^- \qquad \text{(Step 3)}$$

$$MOOH + OH^- \rightarrow M + O_2 + e^- \qquad \text{(Step 4)}$$

While the DS model proceeds via the bimetallic O-O coupling:

$$2\,M = O \rightarrow M + O_2 \qquad \text{(Step 5)}$$

The derivation of Tafel slopes assuming different rate-determining steps is shown in the SI (Section S4.1), while the simulated Tafel slopes are shown in Figure 8a. Different RDSs can be distinguished at low overpotentials, where 120 mV/decade slope is expected when Step 1 is the RDS. The Tafel slopes of 40, 23.6, 16 or 14 mV/decade are expected when Step 2, Step 3, Step 4 or Step 5 is the RDS. Experimental Tafel slopes of the MMO were derived from LSV data (Figure 8b, Figure S15b), illustrating values increasing from 16 mV/decade at 0.07 V overpotential to 180 mV/decade at 0.25 V overpotential. Given that the experimental slope drops below 20 mV/decade at low overpotentials (0.07 V), we hypothesize that the RDS is the release of O_2, either via Step 4 (for the SS mechanism with a Tafel slope of 16 mV/decade) or via Step 5 (for the DS mechanism with a Tafel slope of 14 mV/decade). In this context, the OER bottleneck intermediates are identified to be the formation of either MOOH (for the SS mechanism) or M=O (for the DS mechanism).

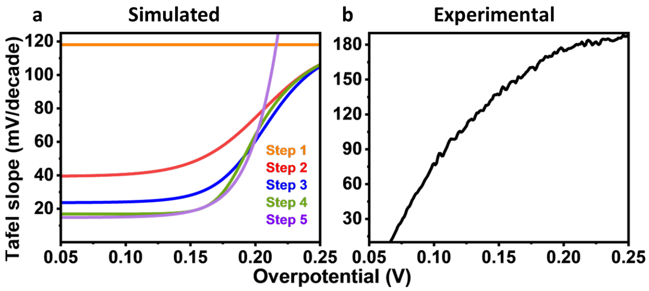

Figure 8. (a) Simulated and (b) experimental Tafel slope analysis for OER.

According to the XAS-EC data, the Co and Cu centers demonstrated chemical and structural evolution during OER (Figures 5 and 6). Notably, only the Co center underwent a change in the oxidation state from Co^{2+} to Co^{3+}, while the Cu centers maintain their original $Cu^{+/2+}$ states. Based on these observations, a SS mechanism was proposed involving Co^{3+}-OOH as the bottleneck intermediate before the RDS of O_2 evolution. As depicted in Figure 9, the catalytic cycle includes cooperative catalysis by a redox-active Co center Co^{2+}-H_2O and redox-innocent Cu. This proposed mechanism is supported by the XAS-EC data, which show the elongation of the Cu-O and the compression of Co-O bond lengths in the intermediate Co^{3+}-OOH, a structural change that is consistent with the increased charge of the Co^{3+} center. This change in the Co-O-Cu bond lengths indicates the mechanism by which the neighboring Cu-atoms tune the reactivity of the Co^{3+}-OOH intermediate, facilitating the evolution of O_2. Previous studies involving mixed metal Co/Cu oxides and sulfides have also reported a synergy between the two metals during OER.[90,91] In general, the synergy was attributed to the modulation of reactive, high-spin O_h Co^{3+} intermediates and these conclusions are in agreement with our experimental observations. Our observation of bond length changes in the Co-O-Cu moiety may be a structural change critical for the formation of either more reactive or more stabilized Co^{3+}-hydroperoxides and may be explored as a criterium for the design of future MMO catalysts.

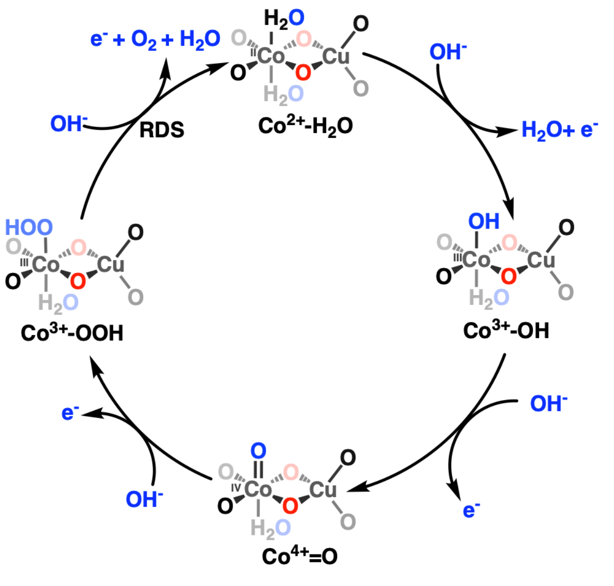

Figure 9. Proposed mechanism of the SS model for OER.

CONCLUSION:

In summary, by employing synchrotron-based XAS, combined with Tafel slope analysis, we reveal the complex catalytic behavior exhibited by the Co-Cu-W MMO@CP under alkaline OER and HER. The HER was found to proceed via operando formation of catalytically active Cu-NPs, electro-generated from the Cu^{+}-oxo pre-catalysts. We also find that the Cu-NPs undergo dynamic evolution during catalysis, with the NP diameter increasing during the first few hours of electrolysis. The OER was found to proceed via a Co^{3+}-OOH bottleneck intermediate, whose electronic behavior and structure is tuned by the neighboring Cu atoms. The identification of key redox-active centers, determination of RDS, and revelation of intermediates, is a substantial leap in our understanding of the fundamental mechanisms of electrocatalytic water splitting driven by mixed metal oxide electrocatalysts. In future, this insight will guide the knowledge-based design of efficient MMO electrocatalysts, and also highlights the importance of synergistic interactions within MMO systems, thereby laying a solid foundation for the design of next-generation electrocatalysts for challenging energy conversion and storage reactions.

ASSOCIATED CONTENT

Supporting Information

Contains materials synthesis and its characterization, experimental details for XAS measurements, Tafel slope derivation for different OER steps.

AUTHOR INFORMATION

Corresponding Author

Ksenija D. Glusac - Department of Chemistry, University of Illinois Chicago, Chicago, Illinois 60607,
United States; Chemical Sciences and Engineering, Argonne National Laboratory, Lemont, Illinois 60439, United States; orcid.org/0000-0002-2734-057X; Email: glusac@uic.edu

Dandan Gao - Department of Chemistry, Johannes Gutenberg University Mainz, Mainz 55128, Germany;
Email: dandan.gao@uni-mainz.de.

Author Contributions

The manuscript was written through contributions of all authors. / All authors have given approval to the final version of the manuscript.

Notes

The authors declare no conflict of interest.

ACKNOWLEDGMENT

This work is supported by the National Science Foundation (CAS 2102247). We also acknowledge support from the Advanced Photon Source, a U.S. Department of Energy (DOE) Office of Science User Facility at Argonne National Laboratory, supported by the U.S. DOE Office of Science-Basic Energy Sciences, under Contract No. DE-AC02-06CH11357. This work was also financially supported by the Deutsche Forschungsgemeinschaft DFG (Walter Benjamin Fellowship, project no. 510966757 and TRR 234 CataLight, project no: 364549901), the German Federal Ministry for Education and Research (BMBF) through the Clusters4Future Initiative (cluster ETOS, project ELFION, project no 03ZU1205EA), the Carl Zeiss Stiftung (project “Halocycles”, project no P2021-10-007) and the Top Level Research Area SusInnoScience of the Federal State of Rheinland-Pfalz.

ABBREVIATIONS

XAS, X-ray Absorption Spectroscopy; XANES, X-ray Absorption Near-Edge structure; EXAFS, extended X-ray Absorption Fine Structure; XAS-EC, X-ray absorption spectro-electrochemistry; RDS, Rate Determining Step; MMO, Mixed Metal Oxide; O_h, Octahedral; T_d, Tetrahedral; SP, Square-planar; Cu-NP, Copper Nanoparticle.

REFERENCES

(1) Ifkovits, Z. P.; Evans, J. M.; Meier, M. C.; Papadantonakis, K. M.; Lewis, N. S. Decoupled Electrochemical Water-Splitting Systems: A Review and Perspective. *Energy and Environmental Science*. Royal Society of Chemistry September 1, 2021, pp 4740–4759. https://doi.org/10.1039/d1ee01226f.

(2) Lamers, P.; Ghosh, T.; Upasani, S.; Sacchi, R.; Daioglou, V. Linking Life Cycle and Integrated Assessment Modeling to Evaluate Technologies in an Evolving System Context: A Power-to-Hydrogen Case Study for the United States. *Environ Sci Technol* **2023**, *57* (6), 2464–2473. https://doi.org/10.1021/acs.est.2c04246.

(3) Geletii, Y. V.; Huang, Z.; Hou, Y.; Musaev, D. G.; Lian, T.; Hill, C. L. Homogeneous Light-Driven Water Oxidation Catalyzed by a Tetraruthenium Complex with All Inorganic Ligands. *J Am Chem Soc* **2009**, *131* (22), 7522–7523. https://doi.org/10.1021/ja901373m.

(4) Yu, M.; Budiyanto, E.; Tüysüz, H. Principles of Water Electrolysis and Recent Progress in Cobalt-, Nickel-, and Iron-Based Oxides for the Oxygen Evolution Reaction. *Angewandte Chemie - International Edition*. John Wiley and Sons Inc January 3, 2022. https://doi.org/10.1002/anie.202103824.

(5) Wang, M.; Wa, Q.; Bai, X.; He, Z.; Samarakoon, W. S.; Ma, Q.; Du, Y.; Chen, Y.; Zhou, H.; Liu, Y.; Wang, X.; Feng, Z. The Restructuring-Induced CoOxCatalyst for Electrochemical Water Splitting. *J Am Chem Soc* **2021**, *1* (12), 2216–2223. https://doi.org/10.1021/jacsau.1c00346.

(6) Huynh, M.; Bediako, D. K.; Nocera, D. G. A Functionally Stable Manganese Oxide Oxygen Evolution Catalyst in Acid. *J Am Chem Soc* **2014**, *136* (16), 6002–6010. https://doi.org/10.1021/ja413147e.

(7) Xu, L.; Jiang, Q.; Xiao, Z.; Li, X.; Huo, J.; Wang, S.; Dai, L. Plasma-Engraved Co 3 O 4 Nanosheets with Oxygen Vacancies and High Surface Area for the Oxygen Evolution Reaction . *Angewandte Chemie* **2016**, *128* (17), 5363–5367. https://doi.org/10.1002/ange.201600687.

(8) Luo, W.; Hu, J.; Diao, H.; Schwarz, B.; Streb, C.; Song, Y.-F. Stabile Polyoxometallat-Nickelschaum-Elektroden Für Elektrochemische Sauerstoffentwicklung Im Alkalischen Milieu. *Angewandte Chemie* **2017**, *129* (18), 5023–5026. https://doi.org/10.1002/ange.201612232.

(9) Zhang, R.; Pan, L.; Guo, B.; Huang, Z. F.; Chen, Z.; Wang, L.; Zhang, X.; Guo, Z.; Xu, W.; Loh, K. P.; Zou, J. J. Tracking the Role of Defect Types in Co3O4 Structural Evolution and Active Motifs during Oxygen Evolution Reaction. *J Am Chem Soc* **2022**. https://doi.org/10.1021/jacs.2c10515.

(10) Lu, X. F.; Gu, L. F.; Wang, J. W.; Wu, J. X.; Liao, P. Q.; Li, G. R. Bimetal-Organic Framework Derived CoFe2O4/C Porous Hybrid Nanorod Arrays as High-Performance Electrocatalysts for Oxygen Evolution Reaction. *Advanced Materials* **2017**, *29* (3). https://doi.org/10.1002/adma.201604437.

(11) Li, N.; Bediako, D. K.; Hadt, R. G.; Hayes, D.; Kempa, T. J.; Von Cube, F.; Bell, D. C.; Chen, L. X.; Nocera, D. G. Influence of Iron Doping on Tetravalent Nickel Content in Catalytic Oxygen Evolving Films. *Proc Natl Acad Sci U S A* **2017**, *114* (7), 1486–1491. https://doi.org/10.1073/pnas.1620787114.

(12) Ling, T.; Zhang, T.; Ge, B.; Han, L.; Zheng, L.; Lin, F.; Xu, Z.; Hu, W. Bin; Du, X. W.; Davey, K.; Qiao, S. Z. Well-Dispersed Nickel- and Zinc-Tailored Electronic Structure of a Transition Metal Oxide for Highly Active Alkaline Hydrogen Evolution Reaction. *Advanced Materials* **2019**, *31* (16). https://doi.org/10.1002/adma.201807771.

(13) Gong, R.; Gao, D.; Liu, R.; Sorsche, D.; Biskupek, J.; Kaiser, U.; Rau, S.; Streb, C. Self-Activation of a Polyoxometalate-Derived Composite Electrocatalyst for the Oxygen Evolution Reaction. *ACS Appl Energy Mater* **2021**, *4* (11), 12671–12676. https://doi.org/10.1021/acsaem.1c02399.

(14) Zhao, Y.; Dongfang, N.; Triana, C. A.; Huang, C.; Erni, R.; Wan, W.; Li, J.; Stoian, D.; Pan, L.; Zhang, P.; Lan, J.; Iannuzzi, M.; Patzke, G. R. Dynamics and Control of Active Sites in Hierarchically Nanostructured Cobalt Phosphide/Chalcogenide-Based Electrocatalysts for Water Splitting. *Energy Environ Sci* **2022**, *15* (2), 727–739. https://doi.org/10.1039/D1EE02249K.

(15) Ling, T.; Zhang, T.; Ge, B.; Han, L.; Zheng, L.; Lin, F.; Xu, Z.; Hu, W. Bin; Du, X. W.; Davey, K.; Qiao, S. Z. Well-Dispersed Nickel- and Zinc-Tailored Electronic Structure of a Transition Metal Oxide for Highly Active Alkaline Hydrogen Evolution Reaction. *Advanced Materials* **2019**, *31* (16). https://doi.org/10.1002/adma.201807771.

(16) She, Z. W.; Kibsgaard, J.; Dickens, C. F.; Chorkendorff, I.; Nørskov, J. K.; Jaramillo, T. F. Combining Theory and Experiment in Electrocatalysis: Insights into Materials Design. *Science*. American Association for the Advancement of Science January 13, 2017. https://doi.org/10.1126/science.aad4998.

(17) Wang, H.; Zhang, K. H. L.; Hofmann, J. P.; de la Peña O'Shea, V. A.; Oropeza, F. E. The Electronic Structure of Transition Metal Oxides for Oxygen Evolution Reaction. *Journal of Materials Chemistry A*. Royal Society of Chemistry September 21, 2021, pp 19465–19488. https://doi.org/10.1039/d1ta03732c.

(18) Xie, X.; Du, L.; Yan, L.; Park, S.; Qiu, Y.; Sokolowski, J.; Wang, W.; Shao, Y. Oxygen Evolution Reaction in Alkaline Environment: Material Challenges and Solutions. *Advanced Functional Materials*. John Wiley and Sons Inc May 1, 2022. https://doi.org/10.1002/adfm.202110036.

(19) Song, F.; Bai, L.; Moysiadou, A.; Lee, S.; Hu, C.; Liardet, L.; Hu, X. Transition Metal Oxides as Electrocatalysts for the Oxygen Evolution Reaction in Alkaline Solutions: An Application-Inspired Renaissance. *J Am Chem Soc* **2018**, *140* (25), 7748–7759. https://doi.org/10.1021/jacs.8b04546.

(20) Grimaud, A.; Hong, W. T.; Shao-Horn, Y.; Tarascon, J. M. Anionic Redox Processes for Electrochemical Devices. *Nature Materials*. Nature Publishing Group January 22, 2016, pp 121–126. https://doi.org/10.1038/nmat4551.

(21) Dau, H.; Limberg, C.; Reier, T.; Risch, M.; Roggan, S.; Strasser, P. The Mechanism of Water Oxidation: From Electrolysis via Homogeneous to Biological Catalysis. *ChemCatChem*. July 12, 2010, pp 724–761. https://doi.org/10.1002/cctc.201000126.

(22) Rossmeisl, J.; Qu, Z. W.; Zhu, H.; Kroes, G. J.; Nørskov, J. K. Electrolysis of Water on Oxide Surfaces. *Journal of Electroanalytical Chemistry* **2007**, *607* (1–2), 83–89. https://doi.org/10.1016/j.jelechem.2006.11.008.

(23) Doyle, R. L.; Lyons, M. E. G. Kinetics and Mechanistic Aspects of the Oxygen Evolution Reaction at Hydrous Iron Oxide Films in Base. *J Electrochem Soc* **2013**, *160* (2), H142–H154. https://doi.org/10.1149/2.015303jes.

(24) Jiao, Y.; Zheng, Y.; Jaroniec, M.; Qiao, S. Z. Design of Electrocatalysts for Oxygen- and Hydrogen-Involving Energy Conversion Reactions. *Chemical Society Reviews*. Royal Society of Chemistry April 21, 2015, pp 2060–2086. https://doi.org/10.1039/c4cs00470a.

(25) Benck, J. D.; Hellstern, T. R.; Kibsgaard, J.; Chakthranont, P.; Jaramillo, T. F. Catalyzing the Hydrogen Evolution Reaction (HER) with Molybdenum Sulfide Nanomaterials. *ACS Catalysis*. American Chemical Society October 8, 2014, pp 3957–3971. https://doi.org/10.1021/cs500923c.

(26) Rüetschi, P.; Delahay, P. Influence of Electrode Material on Oxygen Overvoltage: A Theoretical Analysis. *J Chem Phys* **1955**, *23* (3), 556–560. https://doi.org/10.1063/1.1742029.

(27) Subbaraman, R.; Tripkovic, D.; Chang, K. C.; Strmcnik, D.; Paulikas, A. P.; Hirunsit, P.; Chan, M.; Greeley, J.; Stamenkovic, V.; Markovic, N. M. Trends in Activity for the Water Electrolyser Reactions on 3d M(Ni,Co,Fe,Mn) Hydr(Oxy)Oxide Catalysts. *Nat Mater* **2012**, *11* (6), 550–557. https://doi.org/10.1038/nmat3313.

(28) Morales-Guio, C. G.; Liardet, L.; Hu, X. Oxidatively Electrodeposited Thin-Film Transition Metal (Oxy)Hydroxides as Oxygen Evolution Catalysts. *J Am Chem Soc* **2016**, *138* (28), 8946–8957. https://doi.org/10.1021/jacs.6b05196.

(29) Ogawa, Y.; Hideaki, I.; Takeo, F.; -, al; Liu, X.-D.; Meng, D.-D. *The Electrocatalysis of Oxygen Evolution on Perovskites You May Also like Study on La 2 O 3 Wet Clean by PH Controlled Functional Water Microstructured Hydroxyl Environments and Raman Spectroscopy in Selected Basic Transition-Metal Halides*.

(30) Trasatti, S. Work Function, Electronegativity, and Electrochemical Behaviour of Metals. *J Electroanal Chem Interfacial Electrochem* **1972**, *39* (1), 163–184. https://doi.org/10.1016/S0022-0728(72)80485-6.

(31) Petrii, O. A.; Tsirlina, G. A. Electrocatalytic Activity Prediction for Hydrogen Electrode Reaction: Intuition, Art, Science. *Electrochim Acta* **1994**, *39* (11–12), 1739–1747. https://doi.org/10.1016/0013-4686(94)85159-X.

(32) Conway, B. E.; Jerkiewicz, G. Relation of Energies and Coverages of Underpotential and Overpotential Deposited H at Pt and Other Metals to the 'Volcano Curve' for Cathodic H2 Evolution Kinetics. *Electrochim Acta* **2000**, *45* (25–26), 4075–4083. https://doi.org/10.1016/S0013-4686(00)00523-5.

(33) Fujii, M. S.; Portegies Zwart, S. The Origin of OB Runaway Stars. *Science (1979)* **2011**, *334* (6061), 1380–1383. https://doi.org/10.1126/science.1211927.

(34) Huang, X.; Wang, J.; Tao, H. B.; Tian, H.; Xu, H. An Essential Descriptor for the Oxygen Evolution Reaction on Reducible Metal Oxide Surfaces. *Chem Sci* **2019**, *10* (11), 3340–3345. https://doi.org/10.1039/C8SC04521F.

(35) Hansen, H. A.; Man, I. C.; Studt, F.; Abild-Pedersen, F.; Bligaard, T.; Rossmeisl, J. Electrochemical Chlorine Evolution at Rutile Oxide (110) Surfaces. *Phys. Chem. Chem. Phys.* **2010**, *12* (1), 283–290. https://doi.org/10.1039/B917459A.

(36) Halck, N. B.; Petrykin, V.; Krtil, P.; Rossmeisl, J. Beyond the Volcano Limitations in Electrocatalysis-Oxygen Evolution Reaction. *Physical Chemistry Chemical Physics* **2014**, *16* (27), 13682–13688. https://doi.org/10.1039/c4cp00571f.

(37) Grimaud, A.; May, K. J.; Carlton, C. E.; Lee, Y. L.; Risch, M.; Hong, W. T.; Zhou, J.; Shao-Horn, Y. Double Perovskites as a Family of Highly Active Catalysts for Oxygen Evolution in Alkaline Solution. *Nat Commun* **2013**, *4*. https://doi.org/10.1038/ncomms3439.

(38) Liu, X.; Meng, J.; Zhu, J.; Huang, M.; Wen, B.; Guo, R.; Mai, L. Comprehensive Understandings into Complete Reconstruction of Precatalysts: Synthesis, Applications, and Characterizations. *Advanced Materials* **2021**, *33* (32). https://doi.org/10.1002/adma.202007344.

(39) Zhao, Y.; Adiyeri Saseendran, D. P.; Huang, C.; Triana, C. A.; Marks, W. R.; Chen, H.; Zhao, H.; Patzke, G. R. Oxygen Evolution/Reduction Reaction Catalysts: From *In Situ* Monitoring and Reaction Mechanisms to Rational Design. *Chem Rev* **2023**, *123* (9), 6257–6358. https://doi.org/10.1021/acs.chemrev.2c00515.

(40) Ahn, H. S.; Bard, A. J. Surface Interrogation Scanning Electrochemical Microscopy of Ni$_{1-x}$Fe$_x$OOH (0 < *x* < 0.27) Oxygen Evolving Catalyst: Kinetics of the "Fast" Iron Sites. *J Am Chem Soc* **2016**, *138* (1), 313–318. https://doi.org/10.1021/jacs.5b10977.

(41) Liu, D.; Shadike, Z.; Lin, R.; Qian, K.; Li, H.; Li, K.; Wang, S.; Yu, Q.; Liu, M.; Ganapathy, S.; Qin, X.; Yang, Q.; Wagemaker, M.; Kang, F.; Yang, X.; Li, B. Review of Recent Development of In Situ/Operando Characterization Techniques for Lithium Battery Research. *Advanced Materials* **2019**, *31* (28), 1806620. https://doi.org/10.1002/adma.201806620.

(42) Ortiz Peña, N.; Ihiawakrim, D.; Han, M.; Lassalle-Kaiser, B.; Carenco, S.; Sanchez, C.; Laberty-Robert, C.; Portehault, D.; Ersen, O. Morphological and Structural Evolution of Co$_3$O$_4$ Nanoparticles Revealed by *in Situ* Electrochemical Transmission Electron Microscopy during Electrocatalytic Water Oxidation. *ACS Nano* **2019**, *13* (10), 11372–11381. https://doi.org/10.1021/acsnano.9b04745.

(43) Deng, Y.; Handoko, A. D.; Du, Y.; Xi, S.; Yeo, B. S. *In Situ* Raman Spectroscopy of Copper and Copper Oxide Surfaces during Electrochemical Oxygen Evolution Reaction: Identification of Cu^{III} Oxides as Catalytically Active Species. *ACS Catal* **2016**, *6* (4), 2473–2481. https://doi.org/10.1021/acscatal.6b00205.

(44) Handoko, A. D.; Wei, F.; Jenndy; Yeo, B. S.; Seh, Z. W. Understanding Heterogeneous Electrocatalytic Carbon Dioxide Reduction through Operando Techniques. *Nature Catalysis*. Nature Publishing Group December 1, 2018, pp 922–934. https://doi.org/10.1038/s41929-018-0182-6.

(45) Tung, C.-W.; Hsu, Y.-Y.; Shen, Y.-P.; Zheng, Y.; Chan, T.-S.; Sheu, H.-S.; Cheng, Y.-C.; Chen, H. M. Reversible Adapting Layer Produces Robust Single-Crystal Electrocatalyst for Oxygen Evolution. *Nat Commun* **2015**, *6* (1), 8106. https://doi.org/10.1038/ncomms9106.

(46) Zhu, Y.; Kuo, T.-R.; Li, Y.-H.; Qi, M.-Y.; Chen, G.; Wang, J.; Xu, Y.-J.; Chen, H. M. Emerging Dynamic Structure of Electrocatalysts Unveiled by *in Situ* X-Ray Diffraction/Absorption Spectroscopy. *Energy Environ Sci* **2021**, *14* (4), 1928–1958. https://doi.org/10.1039/D0EE03903A.

(47) Chang, C.-J.; Zhu, Y.; Wang, J.; Chen, H.-C.; Tung, C.-W.; Chu, Y.-C.; Chen, H. M. *In Situ* X-Ray Diffraction and X-Ray Absorption Spectroscopy of Electrocatalysts for Energy Conversion Reactions. *J Mater Chem A Mater* **2020**, *8* (37), 19079–19112. https://doi.org/10.1039/D0TA06656G.

(48) Stoerzinger, K. A.; Hong, W. T.; Crumlin, E. J.; Bluhm, H.; Shao-Horn, Y. Insights into Electrochemical Reactions from Ambient Pressure Photoelectron Spectroscopy. *Acc Chem Res* **2015**, *48* (11), 2976–2983. https://doi.org/10.1021/acs.accounts.5b00275.

(49) Chen, J. Y. C.; Dang, L.; Liang, H.; Bi, W.; Gerken, J. B.; Jin, S.; Alp, E. E.; Stahl, S. S. Operando Analysis of NiFe and Fe Oxyhydroxide Electrocatalysts for Water Oxidation: Detection of Fe^{4+} by Mössbauer Spectroscopy. *J Am Chem Soc* **2015**, *137* (48), 15090–15093. https://doi.org/10.1021/jacs.5b10699.

(50) Reuss, T.; Nair Lalithambika, S. S.; David, C.; Döring, F.; Jooss, C.; Risch, M.; Techert, S. Advancements in Liquid Jet Technology and X-Ray Spectroscopy for Understanding Energy Conversion Materials during Operation. *Acc Chem Res* **2023**, *56* (3), 203–214. https://doi.org/10.1021/acs.accounts.2c00525.

(51) Kim, M.; Park, J.; Ju, H.; Kim, J. Y.; Cho, H.-S.; Kim, C.-H.; Kim, B.-H.; Lee, S. W. Understanding Synergistic Metal–Oxide Interactions of *in Situ* Exsolved Metal Nanoparticles on a Pyrochlore Oxide Support for Enhanced Water Splitting. *Energy Environ Sci* **2021**, *14* (5), 3053–3063. https://doi.org/10.1039/D0EE02935A.

(52) Chen, S.; Ma, L.; Huang, Z.; Liang, G.; Zhi, C. In Situ/Operando Analysis of Surface Reconstruction of Transition Metal-Based Oxygen Evolution Electrocatalysts. *Cell Rep Phys Sci* **2022**, *3* (1), 100729. https://doi.org/10.1016/j.xcrp.2021.100729.

(53) Shackleford, S. G. D.; Boxall, C.; Port, S. N.; Taylor, R. J. An in Situ Electrochemical Quartz Crystal Microbalance Study of Polycrystalline Gold Electrodes in Nitric Acid Solution. *Journal*

of Electroanalytical Chemistry **2002**, *538–539*, 109–119. https://doi.org/10.1016/S0022-0728(02)01218-4.

(54) Risch, M.; Morales, D. M.; Villalobos, J.; Antipin, D. What X-Ray Absorption Spectroscopy Can Tell Us About the Active State of Earth-Abundant Electrocatalysts for the Oxygen Evolution Reaction**. *Angewandte Chemie International Edition* **2022**, *61* (50). https://doi.org/10.1002/anie.202211949.

(55) van Oversteeg, C. H. M.; Doan, H. Q.; de Groot, F. M. F.; Cuk, T. In Situ X-Ray Absorption Spectroscopy of Transition Metal Based Water Oxidation Catalysts. *Chem Soc Rev* **2017**, *46* (1), 102–125. https://doi.org/10.1039/C6CS00230G.

(56) Wang, M.; Árnadóttir, L.; Xu, Z. J.; Feng, Z. In Situ X-Ray Absorption Spectroscopy Studies of Nanoscale Electrocatalysts. *Nanomicro Lett* **2019**, *11* (1), 47. https://doi.org/10.1007/s40820-019-0277-x.

(57) Yang, Y.; Wang, Y.; Xiong, Y.; Huang, X.; Shen, L.; Huang, R.; Wang, H.; Pastore, J. P.; Yu, S.-H.; Xiao, L.; Brock, J. D.; Zhuang, L.; Abruña, H. D. *In Situ* X-Ray Absorption Spectroscopy of a Synergistic Co–Mn Oxide Catalyst for the Oxygen Reduction Reaction. *J Am Chem Soc* **2019**, *141* (4), 1463–1466. https://doi.org/10.1021/jacs.8b12243.

(58) Maurizio, C.; Habra, N. El; Rossetto, G.; Merlini, M.; Cattaruzza, E.; Pandolfo, L.; Casarin, M. XAS and GIXRD Study of Co Sites in CoAl2O4 Layers Grown by MOCVD. *Chemistry of Materials* **2010**, *22* (5), 1933–1942. https://doi.org/10.1021/cm9018106.

(59) Gao, D.; Liu, R.; Biskupek, J.; Kaiser, U.; Song, Y.; Streb, C. Modular Design of Noble-Metal-Free Mixed Metal Oxide Electrocatalysts for Complete Water Splitting. *Angewandte Chemie* **2019**, *131* (14), 4692–4696. https://doi.org/10.1002/ange.201900428.

(60) Neel, J. V.; Schull, W. J.; McDonald, D. J.; Morton, N. E.; Kodani, M.; Takeshima, K.; Anderson, R. C.; Wood, J.; Brewer, R.; Wright, S.; Yamazaki, J.; Suzuki, M.; Kitamura, S. The Effect of Exposure to the Atomic Bombs on Pregnancy Termination in Hiroshima and Nagasaki: Preliminary Report. *Science (1979)* **1953**, *118* (3071), 537–541. https://doi.org/10.1126/science.118.3071.537.

(61) Lv, H.; Song, J.; Geletii, Y. V.; Vickers, J. W.; Sumliner, J. M.; Musaev, D. G.; Kögerler, P.; Zhuk, P. F.; Bacsa, J.; Zhu, G.; Hill, C. L. An Exceptionally Fast Homogeneous Carbon-Free Cobalt-Based Water Oxidation Catalyst. *J Am Chem Soc* **2014**, *136* (26), 9268–9271. https://doi.org/10.1021/ja5045488.

(62) Villars, P.; Cenzual, K.; Daams, J.; Gladyshevskii, R.; Shcherban, O.; Dubenskyy, V.; Kuprysyuk, V.; Savysyuk, I. K5[CoW12O40]·20H2O; 2010; pp 515–516. https://doi.org/10.1007/978-3-642-02702-4_356.

(63) Hilbrig, F.; Gobel, H. E.; Knó, H.; Schmelz, H.; Lengeler, B. *Power Generation Group KWU, Siemens AG, Otto Hahn Ring 6, 8000 München 83*; 1991; Vol. 95. https://pubs.acs.org/sharingguidelines.

(64) Yamazoe, S.; Hitomi, Y.; Shishido, T.; Tanaka, T. XAFS Study of Tungsten L1- And L3-Edges: Structural Analysis of WO3 Species Loaded on TiO2 as a Catalyst for Photo-Oxidation of NH3. *Journal of Physical Chemistry C* **2008**, *112* (17), 6869–6879. https://doi.org/10.1021/jp711250f.

(65) Weng, Z.; Wu, Y.; Wang, M.; Jiang, J.; Yang, K.; Huo, S.; Wang, X.-F.; Ma, Q.; Brudvig, G. W.; Batista, V. S.; Liang, Y.; Feng, Z.; Wang, H. Active Sites of Copper-Complex Catalytic Materials for Electrochemical Carbon Dioxide Reduction. *Nat Commun* **2018**, *9* (1), 415. https://doi.org/10.1038/s41467-018-02819-7.

(66) Khemthong, P.; Photai, P.; Grisdanurak, N. Structural Properties of CuO/TiO2 Nanorod in Relation to Their Catalytic Activity for Simultaneous Hydrogen Production under Solar Light. *Int J Hydrogen Energy* **2013**, *38* (36), 15992–16001. https://doi.org/10.1016/j.ijhydene.2013.10.065.

(67) Gaur, A.; Shrivastava, B. D.; Joshi, S. K. Copper K-Edge XANES of Cu(I) and Cu(II) Oxide Mixtures. *J Phys Conf Ser* **2009**, *190*, 012084. https://doi.org/10.1088/1742-6596/190/1/012084.

(68) Ravel, B.; Newville, M. *ATHENA* , *ARTEMIS* , *HEPHAESTUS* : Data Analysis for X-Ray Absorption Spectroscopy Using *IFEFFIT*. *J Synchrotron Radiat* **2005**, *12* (4), 537–541. https://doi.org/10.1107/S0909049505012719.

(69) Lv, H.; Song, J.; Geletii, Y. V.; Vickers, J. W.; Sumliner, J. M.; Musaev, D. G.; Kögerler, P.; Zhuk, P. F.; Bacsa, J.; Zhu, G.; Hill, C. L. An Exceptionally Fast Homogeneous Carbon-Free Cobalt-Based Water Oxidation Catalyst. *J Am Chem Soc* **2014**, *136* (26), 9268–9271. https://doi.org/10.1021/ja5045488.

(70) Neel, J. V.; Schull, W. J.; McDonald, D. J.; Morton, N. E.; Kodani, M.; Takeshima, K.; Anderson, R. C.; Wood, J.; Brewer, R.; Wright, S.; Yamazaki, J.; Suzuki, M.; Kitamura, S. The Effect of Exposure to the Atomic Bombs on Pregnancy Termination in Hiroshima and Nagasaki: Preliminary Report. *Science (1979)* **1953**, *118* (3071), 537–541. https://doi.org/10.1126/science.118.3071.537.

(71) Wang, M.; Feng, Z. Pitfalls in X-Ray Absorption Spectroscopy Analysis and Interpretation: A Practical Guide for General Users. *Curr Opin Electrochem* **2021**, *30*, 100803. https://doi.org/10.1016/j.coelec.2021.100803.

(72) Sharma, A.; Varshney, M.; Park, J.; Ha, T.-K.; Chae, K.-H.; Shin, H.-J. XANES, EXAFS and Photocatalytic Investigations on Copper Oxide Nanoparticles and Nanocomposites. *RSC Adv* **2015**, *5* (28), 21762–21771. https://doi.org/10.1039/C4RA16217J.

(73) Hsiao, M. C.; Wang, H. P.; Yang, Y. W. EXAFS and XANES Studies of Copper in a Solidified Fly Ash. *Environ Sci Technol* **2001**, *35* (12), 2532–2535. https://doi.org/10.1021/es001374v.

(74) Abeysinghe, D.; Smith, M. D.; Yeon, J.; Tran, T. T.; Paria Sena, R.; Hadermann, J.; Halasyamani, P. S.; zur Loye, H.-C. Crystal Growth and Structure Analysis of $Ce_{18}W_{10}O_{57}$: A Complex Oxide Containing Tungsten in an Unusual Trigonal Prismatic Coordination Environment. *Inorg Chem* **2017**, *56* (5), 2566–2575. https://doi.org/10.1021/acs.inorgchem.6b02710.

(75) Dau, H.; Liebisch, P.; Haumann, M. X-Ray Absorption Spectroscopy to Analyze Nuclear Geometry and Electronic Structure of Biological Metal Centers-Potential and Questions Examined with Special Focus on the Tetra-Nuclear Manganese Complex of Oxygenic Photosynthesis. *Anal Bioanal Chem* **2003**, *376* (5), 562–583. https://doi.org/10.1007/s00216-003-1982-2.

(76) Sprague-Klein, E. A.; He, X.; Mara, M. W.; Reinhart, B. J.; Lee, S.; Utschig, L. M.; Mulfort, K. L.; Chen, L. X.; Tiede, D. M. Photo-Electrochemical Effect in the Amorphous Cobalt Oxide Water Oxidation Catalyst Cobalt–Phosphate (CoPi). *ACS Energy Lett* **2022**, *7* (9), 3129–3138. https://doi.org/10.1021/acsenergylett.2c01560.

(77) Hunault, M.; Vercamer, V.; Haverkort, M. W.; Arrio, M.-A.; Brouder, C.; Calas, G.; Juhin, A. Tracking the Signature of Low Symmetry Environments in the XAS *K* Pre-Edge. *J Phys Conf Ser* **2016**, *712*, 012005. https://doi.org/10.1088/1742-6596/712/1/012005.

(78) Esmaeilirad, M.; Kondori, A.; Song, B.; Ruiz Belmonte, A.; Wei, J.; Kucuk, K.; Khanvilkar, S. M.; Efimoff, E.; Chen, W.; Segre, C. U.; Shahbazian-Yassar, R.; Asadi, M. Oxygen Functionalized Copper Nanoparticles for Solar-Driven Conversion of Carbon Dioxide to Methane. *ACS Nano* **2020**, *14* (2), 2099–2108. https://doi.org/10.1021/acsnano.9b08792.

(79) Frenkel, A. I.; Hills, C. W.; Nuzzo, R. G. A View from the Inside: Complexity in the Atomic Scale Ordering of Supported Metal Nanoparticles. *J Phys Chem B* **2001**, *105* (51), 12689–12703. https://doi.org/10.1021/jp012769j.

(80) Frenkel, A. Solving the 3D Structure of Metal Nanoparticles. *Z Kristallogr Cryst Mater* **2007**, *222* (11), 605–611. https://doi.org/10.1524/zkri.2007.222.11.605.

(81) Clausena, B. S.; Topsøe, H.; Hansen, L. B.; Stoltze, P.; Nørskov, J. K. Determination of Metal Particle Sizes from EXAFS. *Catal Today* **1994**, *21* (1), 49–55. https://doi.org/10.1016/0920-5861(94)80033-2.

(82) Durst, J.; Siebel, A.; Simon, C.; Hasché, F.; Herranz, J.; Gasteiger, H. A. New Insights into the Electrochemical Hydrogen Oxidation and Evolution Reaction Mechanism. *Energy Environ. Sci.* **2014**, *7* (7), 2255–2260. https://doi.org/10.1039/C4EE00440J.

(83) Sheng, W.; Zhuang, Z.; Gao, M.; Zheng, J.; Chen, J. G.; Yan, Y. Correlating Hydrogen Oxidation and Evolution Activity on Platinum at Different PH with Measured Hydrogen Binding Energy. *Nat Commun* **2015**, *6* (1), 5848. https://doi.org/10.1038/ncomms6848.

(84) Anantharaj, S.; Noda, S.; Jothi, V. R.; Yi, S.; Driess, M.; Menezes, P. W. Strategies and Perspectives to Catch the Missing Pieces in Energy-Efficient Hydrogen Evolution Reaction in Alkaline Media. *Angewandte Chemie International Edition* **2021**, *60* (35), 18981–19006. https://doi.org/10.1002/anie.202015738.

(85) Huang, C.; Sasaki, K.; Senthil Raja, D.; Hsieh, C.; Wu, Y.; Su, J.; Cheng, C.; Cheng, P.; Lin, S.; Choi, Y.; Lu, S. Twinning Enhances Efficiencies of Metallic Catalysts toward Electrolytic Water Splitting. *Adv Energy Mater* **2021**, *11* (46). https://doi.org/10.1002/aenm.202101827.

(86) Ye, L.; Wen, Z. Self-Supported Three-Dimensional Cu/Cu_2O–CuO/RGO Nanowire Array Electrodes for an Efficient Hydrogen Evolution Reaction. *Chemical Communications* **2018**, *54* (49), 6388–6391. https://doi.org/10.1039/C8CC02510J.

(87) Putra, R. P.; Horino, H.; Rzeznicka, I. I. An Efficient Electrocatalyst for Oxygen Evolution Reaction in Alkaline Solutions Derived from a Copper Chelate Polymer via In Situ Electrochemical Transformation. *Catalysts* **2020**, *10* (2), 233. https://doi.org/10.3390/catal10020233.

(88) Kumar, B.; Saha, S.; Ojha, K.; Ganguli, A. K. A Facile One Step Synthesis of Cu/Cu2O Nanocomposites: Enhanced Hydrogen/Oxygen Evolution. *Mater Res Bull* **2015**, *64*, 283–287. https://doi.org/10.1016/j.materresbull.2014.10.076.

(89) Shinagawa, T.; Garcia-Esparza, A. T.; Takanabe, K. Insight on Tafel Slopes from a Microkinetic Analysis of Aqueous Electrocatalysis for Energy Conversion. *Sci Rep* **2015**, *5* (1), 13801. https://doi.org/10.1038/srep13801.

(90) Yang, H.; Gao, S.; Rao, D.; Zhang, C.; Zhou, X.; Yang, S.; Ye, J.; Yang, S.; Lai, F.; Yan, X. Non-Metallic Electronic Regulation in CuCo Oxy-/Thio-Spinel as Advanced Oxygen Evolution Electrocatalysts. *Sci China Chem* **2021**, *64* (1), 101–108. https://doi.org/10.1007/s11426-020-9895-2.

(91) Chauhan, M.; Reddy, K. P.; Gopinath, C. S.; Deka, S. Copper Cobalt Sulfide Nanosheets Realizing a Promising Electrocatalytic Oxygen Evolution Reaction. *ACS Catal* **2017**, *7* (9), 5871–5879. https://doi.org/10.1021/acscatal.7b01831.

Insert Table of Contents artwork here

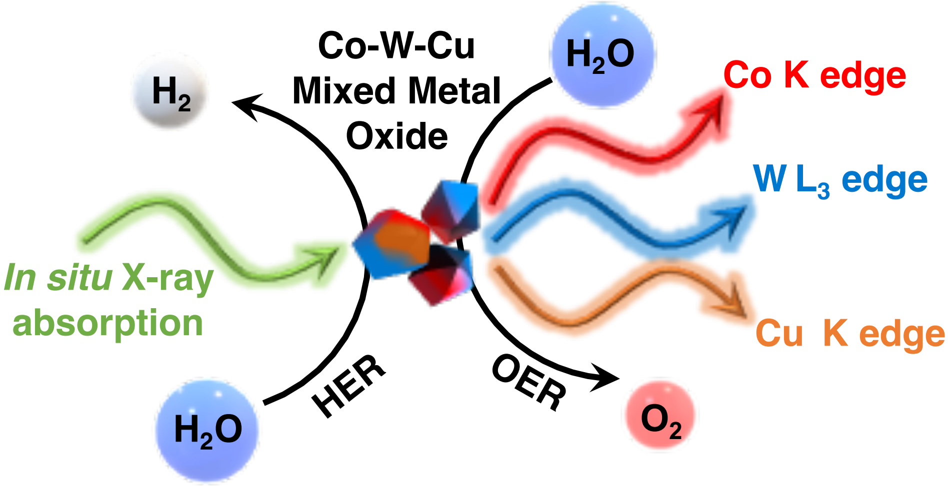

For Table of Contents Only.